

Cosmological constraints using Minkowski functionals from the first year data of the Hyper Suprime-Cam.

Joaquin Armijo,^{1,2}★ Gabriela A. Marques,^{3,4} Camila P. Novaes,^{5,1,2} Leander Thiele,^{1,2} Jessica A. Cowell,^{1,2,6} Daniela Grandón,⁷ Masato Shirasaki,^{8,9} Jia Liu,^{1,2}

¹Kavli Institute for the Physics and Mathematics of the Universe (WPI),

The University of Tokyo Institutes for Advanced Study (UTIAS), The University of Tokyo, Chiba 277-8583, Japan

²Center for Data-Driven Discovery, Kavli IPMU (WPI), UTIAS, The University of Tokyo, Kashiwa, Chiba 277-8583, Japan

³Fermi National Accelerator Laboratory, Batavia, IL 60510, USA

⁴Kavli Institute for Cosmological Physics, University of Chicago, Chicago, IL 60637, USA

⁵Instituto Nacional de Pesquisas Espaciais, Av. dos Astronautas 1758, Jardim da Granja, São José dos Campos, SP, Brazil

⁶Department of Physics, University of Oxford, Denys Wilkinson Building, Keble Road, Oxford OX1 3RH, United Kingdom

⁷Mathematical Institute, Leiden University, Snellius Gebouw, Niels Bohrweg 1, NL-2333 CA Leiden, The Netherlands

⁸National Astronomical Observatory of Japan, National Institutes of Natural Science, Mitaka, Tokyo 181-8588, Japan

⁹The Institute of Statistical Mathematics, Tachikawa, Tokyo 190-8562, Japan

Accepted XXX. Received YYY; in original form ZZZ

ABSTRACT

We use Minkowski functionals to analyse weak lensing convergence maps from the first-year data release of the Subaru Hyper Suprime-Cam (HSC-Y1) survey. Minkowski functionals provide a description of the morphological properties of a field, capturing the non-Gaussian features of the Universe matter-density distribution. Using simulated catalogs that reproduce survey conditions and encode cosmological information, we emulate Minkowski functionals predictions across a range of cosmological parameters to derive the best-fit from the data. By applying multiple scales cuts, we rigorously mitigate systematic effects, including baryonic feedback and intrinsic alignments. From the analysis, combining constraints of the angular power spectrum and Minkowski functionals, we obtain $S_8 \equiv \sigma_8 \sqrt{\Omega_m/0.3} = 0.808^{+0.033}_{-0.046}$ and $\Omega_m = 0.293^{+0.157}_{-0.043}$. These results represent a 40% improvement on the S_8 constraints compared to using power spectrum only. Minkowski functionals results are consistent with other two-point, and higher order statistics constraints using the same data, being in agreement with CMB results from the Planck S_8 measurements. Our study demonstrates the power of Minkowski functionals beyond two-point statistics to constrain and break the degeneracy between Ω_m and σ_8 .

Key words: Cosmology: cosmological parameters, Cosmology - observations

1 INTRODUCTION

The large-scale structure of the Universe is the result of the evolution of matter fluctuations, which is well described by the Λ CDM model. At late times, the underlying matter density field creates large gravitational potentials that can be probed by the bending of light from background galaxies. The primary manifestation of this bending or lensing effect is referred to as cosmic shear (see Kilbinger (2015) and Mandelbaum (2018) for recent reviews), which is understood as the distortion and magnification of the observed galaxy shapes. The Stage-III¹ galaxy surveys observing millions of extragalactic objects, such as Kilo-Degree Survey (KiDS; Hildebrandt et al. 2020; Giblin et al. 2021), the Dark Energy Survey (DES; Dark Energy Survey Collaboration et al. 2016; Troxel et al. 2018; Amon et al. 2022), and the Hyper-Suprime Camera survey (HSC; Hikage et al. 2019; Li

et al. 2022), are used to constrain the Universe at late times. However, the constrained S_8 parameter, defined as $S_8 \equiv \sigma_8(\Omega_m/0.3)^{0.5}$, with Ω_m the matter energy density, and σ_8 the fictitious standard deviation of matter fluctuations in spheres of $8h^{-1}$ Mpc if they had evolved linearly, is in small discrepancy. This disagreement arises when comparing galaxy lensing measurements with the value inferred from observations of the primordial Cosmic Microwave Background (CMB) (Planck Collaboration et al. 2020; Bianchini et al. 2020) as well as quasi-linear matter clustering (CMB lensing) (Madhavacheril et al. 2020).

Over the last decade, various explanations have emerged to address the S_8 discrepancy, including important systematic effects in galaxy surveys, such as photometric redshift estimations (Hildebrandt et al. 2017) and shear calibrations (Melchior & Viola 2012). Nevertheless, their impact has been studied comprehensively, and it is unlikely to account for the total S_8 difference (Hildebrandt et al. 2021; Mandelbaum et al. 2018). The source of this discrepancy still remains an open question, which could reveal unaccounted systematic effects or

★ E-mail: joaquin.armijo@ipmu.jp

¹ Stage-III definition introduced by the Dark Energy Task Force report (Albrecht et al. 2006).

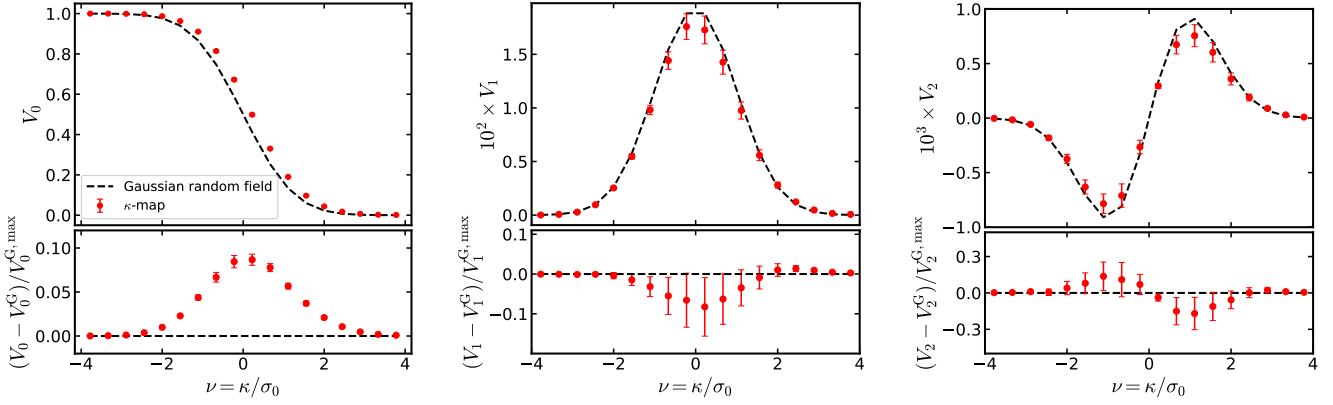


Figure 1. Minkowski Functionals V_0 (left), V_1 (middle) and V_2 (right) as function of κ scaled by the standard deviation of the fiducial kappa maps, σ_0 , calculated for the HSC-Y1 data using a $\theta = 2'$ Gaussian smoothing scale, using the galaxies in the third tomographic redshift bin. Top: The calculations of HSC-Y1 κ -maps (red dots), and predictions from Minkowski functionals assuming a Gaussian random field (GRF; dashed line). Bottom: The difference between the data measurements and Gaussian predictions $V_k - V_k^G$ divided by the maximum of the Gaussian prediction $V_k^{G, \max}$ to help the visualization of the non-Gaussian features. The uncertainties for our V_0 , V_1 , and V_2 measurements (red error bars) are calculated using the covariance matrix from our simulations.

the need of complementary modeling to include smaller scales for the current measurements.

The statistical properties of the matter density field at late times are non-Gaussian, which makes the study of methods beyond two-point statistics indispensable for capturing the information from non-linear scales. Several measurements probing the shear and convergence field have been proposed in the last decade, including the bispectrum and three-point function (Takada & Jain 2003; Fu et al. 2014; Halder et al. 2023), the Probability Distribution Function (PDF) (Liu & Madhavacheril 2019; Boyle et al. 2021; Giblin et al. 2021; Thiele et al. 2023; Anbajagane et al. 2023), measurements of peaks and minima (Davies et al. 2022; Zürcher et al. 2022; Liu et al. 2023a; Marques et al. 2024), density split statistic (Gruen et al. 2018; Burger et al. 2023; Paillas et al. 2024), Minkowski functionals (Marques et al. 2019), Betti numbers (Feldbrugge et al. 2019), and scattering transforms (Cheng et al. 2024; Valogiannis et al. 2024; Gatti et al. 2024). Also, methods employing deep learning such as convolutional neural networks (Fluri et al. 2018; Gupta et al. 2018; Fluri et al. 2022; Zhong et al. 2024) are equally competitive to recover the non-Gaussian information stored in the non-linear matter field. In this paper, we evaluate the application of Minkowski functionals using data from the HSC year 1 dataset.

Minkowski functionals provide an algebraic description of the geometrical properties of a field (Mecke et al. 1994). In cosmology, they measure the features of the patterns formed by large-scale structure of the Universe (Schmalzing et al. 1996; Schmalzing & Buchert 1997). Such patterns trace the distribution of matter of the Universe, being sensitive to the higher-order moments of the matter density field (Sato et al. 2001). Recently, Minkowski functionals have been used for studies of non-linear features in the CMB (Lim & Simon 2012; Novaes et al. 2016; Duque et al. 2024; Hamann & Kang 2024), anisotropies in the distribution of galaxies (Hikage et al. 2003; Appleby et al. 2022), constraints on neutrino masses (Marques et al. 2019; Liu et al. 2023b), studies of HI gas distribution using 21-cm intensity mapping (Spina et al. 2021; Schimd et al. 2024), and modified gravity (Shirasaki et al. 2017; Jiang et al. 2024). In addition, Minkowski functionals are known as a novel and efficient probe for primordial non-Gaussianity as showed in Hikage et al. (2006, 2008a,b); Hikage & Matsubara (2012); Shirasaki et al. (2012). For weak lensing studies, Minkowski functionals have been proposed

to break the degeneracy between Ω_m and σ_8 inherent in two-point statistics (Matsubara & Jain 2001). Moreover, more studies using Minkowski functionals on weak lensing fields provide insight on constraining cosmology beyond power spectrum (Kratochvil et al. 2012; Shirasaki & Yoshida 2014; Petri et al. 2015; Grewal et al. 2022), including measurements using the Canada-France-Hawaii Lensing Survey (CFHTLenS; Heymans et al. 2012) data. However, the analysis from Petri et al. (2015) finds important biases in the (Ω_m, σ_8) parameter-space. In this paper, we present cosmological constraints derived from Minkowski functionals to evaluate the power of this statistic using the first-year HSC weak lensing data, and to confirm whether the trends observed in these previous studies.

This paper is organized as follows: In Section 2 we describe the application of Minkowski functionals to weak lensing maps. The used data of the HSC-Y1 survey is explained in Section 3. We describe the simulations for making our predictions in Section 4. We provide a description of our modeling of Minkowski functionals using simulations in Section 5. We comment in the analysis of the studied systematics in section 6. The results are presented in Section 7. Finally we summarize the results and draw conclusions in Section 8.

2 MINKOWSKI FUNCTIONALS

Minkowski Functionals correspond to $d + 1$ independent and unique functions, with d the number of dimensions, that describe the geometrical properties of a mathematical space. These functions or “gauges” measure the size, shape and connectivity of a manifold. In the specific case of convergence κ -maps, which is a two-dimensional pixelated space, $d = 2$, these properties are the Area V_0 , Perimeter V_1 and Genus V_2 , which combines the Euler characteristic of the connected pixels or “Island”, and the number of holes in the same space. These are measured in the normalized area A (in our case, the sum of the area of all pixels) and can be defined as:

$$V_0 = \frac{1}{A} \int_{\Sigma(\nu)} da, \quad (1)$$

$$V_1 = \frac{1}{4A} \int_{\partial\Sigma(\nu)} dl, \quad (2)$$

$$V_2 = \frac{1}{2\pi A} \int_{\partial\Sigma(\nu)} \mathcal{K} dl, \quad (3)$$

where da and dl are the area and length elements, respectively, \mathcal{K} is the curvature of the boundary, and $\partial\Sigma(\nu)$ denotes the excursion set boundary. For the κ -field we measured over the surface $\Sigma(\nu)$ with $\nu > \kappa/\sigma_0$, which is defined as a threshold for every value of κ , divided by the standard deviation σ_0 of simulated convergence maps in the fiducial cosmology.

A few studies have described Minkowski functionals calculations for weak lensing convergence maps. Kratochvil et al. (2012) describe the computation of Minkowski functionals for 2D pixelated weak lensing fields as robust, containing valuable non-Gaussian information. Even though the continuum underlying matter density is unknown and the Minkowski functionals can be noisy for a large pixel array, the integral over the amount of information is stable and informative, resulting in a reliable estimator. Each Minkowski functional provides information that can be qualitatively described as explained in Kratochvil et al. (2012): V_0 measure the cumulative distribution function (CDF) of the histogram for the pixel values of the maps (sensitive to the distribution of peaks). V_1 includes a delta function over the convergence values, which measure individual shapes of objects given a value of κ . V_2 measures the same shapes and their connectivity. However, none of these functions consider the spatial distribution of the pixel values, which is encapsulated by the power spectrum, making the information complementary between the two types of statistics. In such setup, the combination of power spectrum and Minkowski functionals should provide tighter constraints for both σ_8 and Ω_m parameters as shown in Kratochvil et al. (2012); Petri et al. (2013); Shirasaki & Yoshida (2014); Marques et al. (2019); Grewal et al. (2022).

The shapes of the Minkowski functionals as function of ν are shown in Figure 1. We compare measurements of the Minkowski functionals from the HSC-Y1 data (red dots), and their analytical predictions obtained from Gaussian random fields (Adler 2014; Tomita 1986; Schmalzing & Buchert 1997) (black dashed lines), using 18 equally spaced bins in the range $-4 < \nu < 4$. For this comparison, we calculated the difference between the Minkowski functionals calculated from the data, and their predictions assuming a Gaussian random field $V_k - V_k^G$ (bottom panels), with $i = 0, 1, 2$. This difference reveals the non-Gaussian information nature of the data and can be predicted for the perturbative non-Gaussian case (Matsubara 2003). Most differences can be found when comparing V_0 , noticing features deviating from the Gaussian predictions for $\nu > -2$, being largely deviated for the high values of $\nu = 0$. For our κ measurements this difference seems to follow a simpler profile proportional to $e^{-\nu^2/2}$ (dotted line). In general, the features showed by V_0 , V_1 and V_2 are consistent with the ones found in Petri et al. (2013), showing that the difference $V_i - V_i^G$ does not converge to the perturbative non-Gaussian case for small smoothing scales, like the ones used throughout this study.

3 HSC YEAR ONE WEAK LENSING DATA

We use the weak lensing shear catalogues from HSC-Y1 (Mandelbaum et al. 2017) with redshift estimated from the HSC five

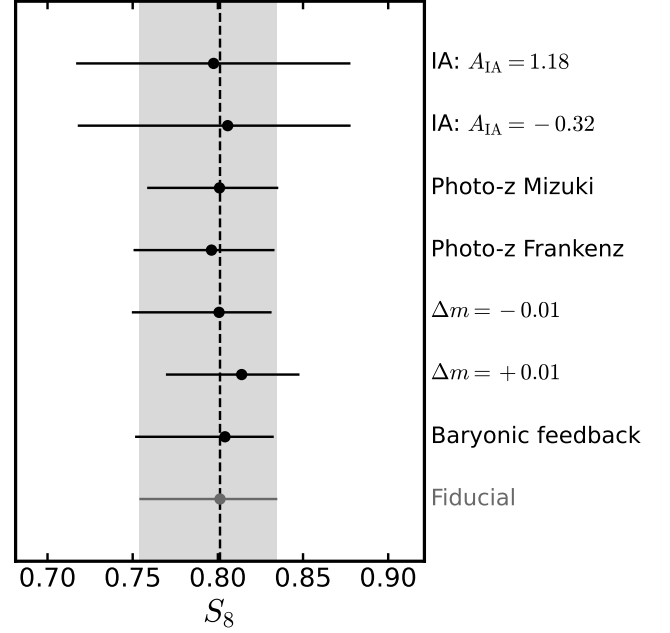


Figure 2. Analysis of the impact of several systematic effects in the inference of the S_8 parameter. Considering the fiducial value (dashed line), we contaminate the data vector with a systematic as labeled in the text. Then we use this new ‘observation’ (black dot with error bar) to repeat the inference in these new values for S_8 . We add the recovered fiducial inference data point (grey dot) and the 68% confidence interval (shaded area) to visually help the comparison.

broad-band photometry using the MLZ code (Tanaka et al. 2018). Then we applied tomographic redshift cuts in 4 bins with edges [0.3, 0.6, 0.9, 1.2, 1.5], but neglecting the fourth redshift bins due to an unknown systematic error found prior to un-blinding. For example, the impact of including this tomographic redshift bin is shown in (Thiele et al. 2023), where a more significant shift on higher S_8 is found for the PDF analysis. Gaussian smoothing is performed over the shear maps with different smoothing scales, using $\theta_s = 1, 2, 4, 5, 8, 10$ arcmin ($''$). Such scales are chosen to study the non-Gaussian features of the κ -maps, while mitigating possible systematic effects at small scales, such as baryonic physics. Finally, we go from tangential shear to the flat-sky convergence κ maps using the Kaiser-Squires inversion method (KS; Kaiser & Squires 1993), after applying map in-painting on the masked pixels (Pires et al. 2009; Starck et al. 2021) to reduce undesired artifacts created by the survey mask. A detailed description of the convergence field reconstruction can be found in Marques et al. (2024).

4 SIMULATIONS

To study the non-Gaussian signal provided by the non-linear evolution of the field we use numerical simulations. These N-body simulations are divided into two sets: One set is used to calculate the covariance matrix and test different systematic effects in our measurements, which is defined as the fiducial cosmology. The second, is a suite of simulations with 100 different cosmologies for emulation.

For the calculations of the covariance matrix, simulations come from a set of 108 quasi independent full-sky simulations (Takahashi et al. 2017), which are utilized to make 2268 mock map realiza-

tions of the HSC-Y1 shape catalogues with a fiducial cosmology ($\Omega_m = 0.297$ and $\sigma_8 = 0.82$) obtained from the Wilkinson Microwave Anisotropy Probe nine-year data (Hinshaw et al. 2013). Mock realizations account for many survey properties (including the survey mask) following the methodology of Shirasaki et al. (2019).

To create the Minkowski functionals predictions from different cosmology values, we use simulations from Shirasaki et al. (2021), which provide ray-traced maps that are used to create mock catalogues based on these simulations with 100 pairs of Ω_m and S_8 values (the remaining cosmological parameters are fixed from the fiducial cosmology). Each cosmology-varied simulation includes different observers in the periodic box to obtain 50 quasi-independent realizations. The same procedure to include observational aspects to the fiducial set is implemented to obtain the final cosmology-varied simulations. The full methodology to create the mock catalogues and convergence maps from the simulations is explained in Marques et al. (2024) and it has been used in previous studies of non-Gaussian statistics (Thiele et al. 2023; Cheng et al. 2024; Grandón et al. 2024; Novaes et al. 2024).

5 MINKOWSKI FUNCTIONALS APPLICATION TO HSC-Y1 DATA

In this section, we overview the methodology to calculate Minkowski functionals in the HSC-Y1 data, including the model predictions, the covariance matrix and the defined likelihood for the inferred posterior. As mentioned in Marques et al. (2024), we follow a blind procedure, using simulations to test the pipeline and define our baseline analysis by selecting smoothing lengths and scale cuts on the data vector.

5.1 Emulator for Minkowski functionals

An emulator for our summary statistic is designed from the cosmology-varied simulations using Gaussian process regression (GPR). Using a slightly modified function than the one used in Marques et al. (2024), with a different radial basis kernel value, we emulate the data vector using the mean of the 50 realizations for each cosmology (out of 100 cosmology pairs). Then we are able to produce emulated Minkowski functionals and the angular power spectrum data vector from a given cosmology pair with a determined accuracy. To validate the emulator, we use the “leave-one-out” method, where the emulator is trained using 99 cosmology pairs, predicting the one not used for training. After testing, the emulator can obtain accurate (between 2 – 3% of differences) model predictions for the Minkowski functionals in an unbiased way. The accuracy decreases for the bins on the extremes of the data vector (low and high tail values of kappa), which suffer more from statistical errors like sample variance and shot noise, but not higher than 5% in average.

5.2 Likelihood estimation

Considering the large number of bins of the combined statistics, which includes the power spectrum and Minkowski functionals for the three tomographic bins and several smoothing scales, we use MOPED compression (Heavens et al. 2000, 2017) and Gaussian likelihood approximation for the inference analysis. First, we define the compressed data vector, which approximately preserves information from the original Minkowski functional data vectors, while reducing its dimensionality to the number of free parameters we are trying to infer (Ω_m and S_8). By compressing the data vector, the likelihood is

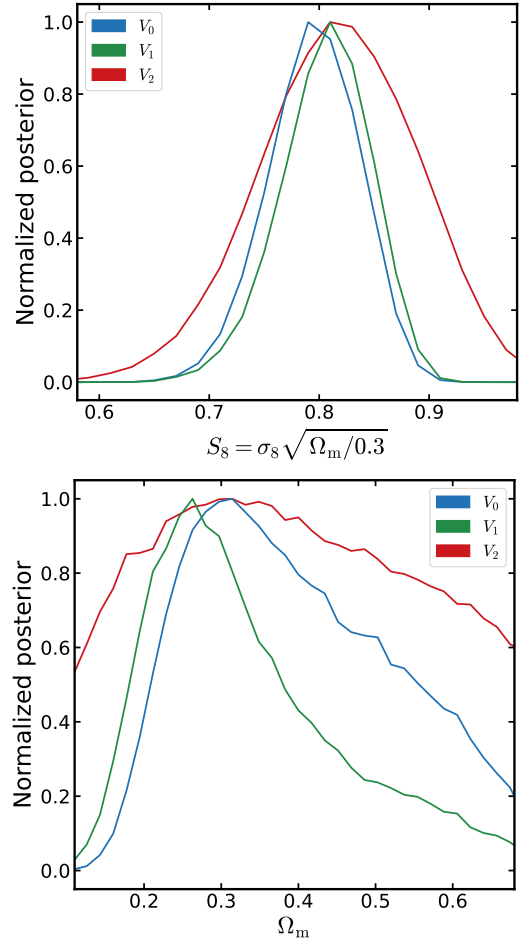


Figure 3. Individual posteriors of S_8 (top) and Ω_m (bottom) parameters using the individual Minkowski functionals: V_0 (blue line), V_1 (green line) and V_2 (red line). Most of the S_8 information is contained in V_0 (area) and V_1 (perimeter) with a improved constraints on Ω_m for V_1 .

close to a Gaussian distribution, due to central limit theorem. In addition, the power spectrum in our analysis is measured for a multipole scale of $300 < \ell < 1000$, in four data bins, also with a likelihood which is well approximated by a Gaussian distribution. Then the combined likelihood is then defined as:

$$-2 \log \mathcal{L} = (\mathbf{x} - \boldsymbol{\mu}(\boldsymbol{\theta}))^\top \boldsymbol{\Sigma}^{-1} (\mathbf{x} - \boldsymbol{\mu}(\boldsymbol{\theta})), \quad (4)$$

where \mathbf{x} is the vector measured on the data, $\boldsymbol{\mu}(\boldsymbol{\theta})$ is the prediction from the emulator for the cosmological parameter vector $\boldsymbol{\theta}$, and $\boldsymbol{\Sigma}^{-1}$ is the inverted covariance matrix from the fiducial simulations. For the data vector \mathbf{x} we use the weighted averaged on all the HSC-Y1 fields, as described in Marques et al. (2024).

The sampling is performed using the publicly available code COBAYA,² which creates Monte Carlo Markov Chain samples using the Metropolis-Hasting algorithm. We use uniformly distributed priors for the cosmological parameters, $0.11 < \Omega_m < 0.65$ and $0.5 < S_8 < 1.1$, which is fairly covered by the cosmology-varied simulations.

² <https://github.com/CobayaSampler>

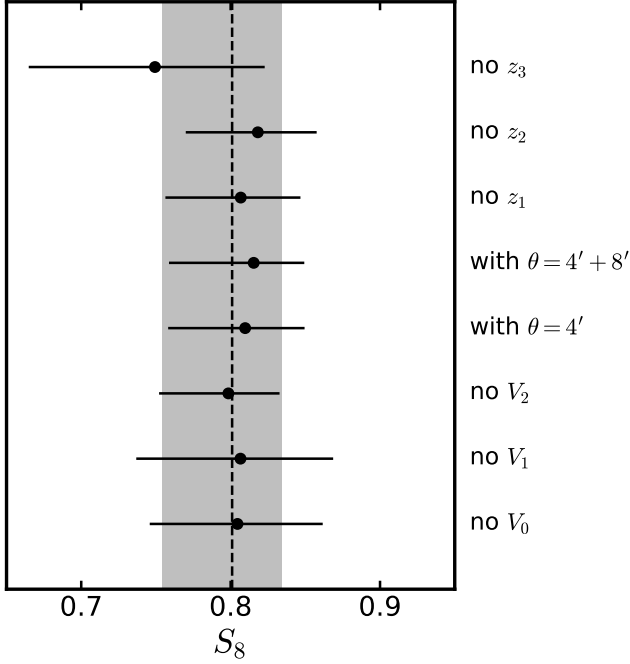


Figure 4. Consistency check testing the different choices of the used data vectors for calculating the posterior of S_8 (black points and lines) contrasted with the baseline results (dashed line) including the 68% confidence interval (grey shaded area).

6 SYSTEMATIC EFFECTS

We test the impact of systematic effects that are not included in the modelling and can potentially bias the final result of our cosmological inference pipeline. These physical effects can be added as contamination directly on the data vector. To take into account errors in calibration, we add a shifting of $\pm 1\%$ in the multiplicative bias factor, which correspond to the uncertainty measured from simulations (Mandelbaum et al. 2018). We also include different photometric redshift estimation codes (FRANKENZ and MIZUKI) in our pipeline. To study the possible shift on S_8 due baryonic effects, we calculate the Minkowski functionals on the κ TNG dataset (Osato et al. 2021), which consists of a set of 10,000 convergence maps using dark matter only (DMO) and hydrodynamic simulations from the IllustrisTNG model (Nelson et al. 2019). Then, we multiply our data vector by the ratio of our calculations, which tells what scales in our statistic are more affected by the effect of baryonic physics. Similarly, the effect of intrinsic alignments (IA) is added from mock shape catalogues infused with the non-linear tidal alignment model (NLA; Bridle & King 2007), with $A_{IA} = 1.18$ and $A_{IA} = -0.32$ (Harnois-Déraps et al. 2021), where we compare the statistics for the mocks with and without the effect of IA, adding the ratio to the fiducial data vector. We do this comparison for results of the $\theta = 2'$ Gaussian kernel smoothed map, which is our baseline analysis, and provides enough information of non-Gaussian statistics. The results of the individual impact for each systematic applied to the fiducial cosmology statistic are shown in Figure 2. We find no significant deviation from the fiducial value of S_8 for the studied systematic effects, finding values between 0.05 - 0.38σ for such shift. However, the initial inference analysis revealed a systematic effect for the individual Minkowski functional V_0 at the first redshift bin z_1 , showing significantly wider contours, which are preserved when combined with V_1 and V_2 . To

solve this particular issue, we keep the last 4 ν bins of this data vector. We select this cut after checking that V_0 at z_1 has negligible constraining power and the posteriors of our final blind analysis is unchanged. We decide by consistently applying scale cuts on the tails of V_0 , V_1 and V_2 in all redshift bins, removing the first and last bins of each individual data vector (with the exception of V_0 at z_1).

7 RESULTS

We check for the individual constraining power of V_0 , V_1 and V_2 , and different data vector combinations to test the robustness of our constraints. Then, we present the unblinded results after applying the scale cuts to avoid the impact of the systematic effects, showing the final constraints for angular power spectrum, Minkowski functionals and the combined statistics.

7.1 Individual Minkowski functional contribution

We provide constraints of individual Minkowski functionals for the fiducial cosmology as a target, trying to discern if there is any specific function that outperforms the others, instead of combining them. We show their comparison in Figure 3, where the 1D marginal posterior of S_8 (top) and Ω_m (bottom) are plotted for the individual Minkowski functionals: V_0 (blue line), V_1 (green line) and V_2 (red line). These show a better performance of V_1 for constraining Ω_m , but individually similar results for both the area and perimeter, and wider constraint provided by the genus function V_2 , meaning that V_0 and V_1 contain more non-Gaussian information than V_2 . Additionally, we notice the constraining power of V_2 is at the level of power spectrum, which is opposite to what is found in (Kratochvil et al. 2012), where genus has similar constraining power compared with V_0 and V_1 . However, their analysis is based on Fisher forecast, where the statistical errors are neglected and the contours can be overconfident. In the same line, V_0 is expected to contain information from the 1-point function measured by the PDF of κ . Indeed, by comparing the 1σ values from the V_0 , we find $S_8 = 0.799^{+0.036}_{-0.045}$ consistent with some of the results presented on Thiele et al. (2023), specifically when PDF is combined with two-point statistics. We also find $S_8 = 0.816^{+0.029}_{-0.051}$ for V_1 and $S_8 = 0.818^{+0.069}_{-0.070}$ for V_2 .

7.2 Consistency checks

We investigate how small variations in the choice of the data vector impact our cosmological constraints. For this, we implement some consistency checks performed by previous analyses applying non-Gaussian statistics to HSC data (Thiele et al. 2023; Marques et al. 2024; Cheng et al. 2024; Novaes et al. 2024). We provide a simple test of consistency in Figure 4, where from the baseline analysis using $\theta = 2'$, we remove individual Minkowski functionals, add an individual smoothing scales of $\theta = 4'$ and $\theta = 8'$, and remove each of the tomographic redshift bins. By comparing with the obtained baseline constraint (dashed line and grey area), we list the different choices of the constraints obtained by the new data vectors. No substantial shift (higher than 1σ) from the baseline result is found if we consider the uncertainties of each data point, even though there is an important shift towards smaller S_8 value once the third redshift bin (z_3) is removed from the analysis. These results show consistency with the analysis from Marques et al. (2024) and Thiele et al. (2023), where the same tendency is found using different statistic, and from Novaes et al. (2024) which also uses Minkowski functionals data.

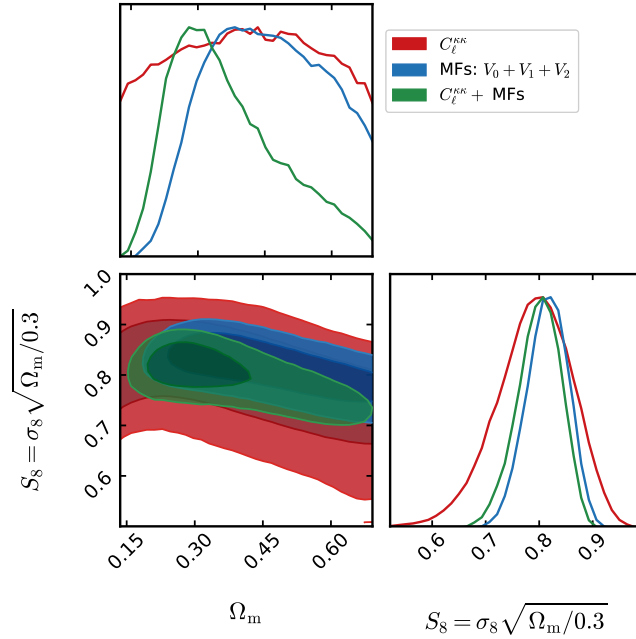


Figure 5. Constraints of Minkowski functionals for Ω_m and $S_8 = \sigma_8 \sqrt{\Omega_m/0.3}$ parameters using the HSC-Y1 data. The inferred posterior is calculated using the angular power spectrum C_ℓ^{KK} (red), the three Minkowski functionals (blue) and the joint measurement using both statistics (green). We colour the 68% (inner line) and 95% (outer line) confidence intervals contours.

Additionally, we find that the data vector including larger smoothing scales, obtains slightly higher S_8 values, but with a larger uncertainty. Opposite tendency is found in [Kratovich et al. \(2012\)](#) (again, using Fisher forecast), where the combination of several smoothing scales improve the constraints.

Finally, removing individual Minkowski functionals complements the results of Figure 3, where we found that V_0 and V_1 have more constraining power than V_2 . These results reaffirm that slightly tighter constraints are provided by $V_0 + V_1$, and V_2 provides less information. We also report marginally wider constraints when removing V_1 from the data vector.

7.3 Angular power spectrum and Minkowski functional constraints

Figure 5 shows the constraints for S_8 and Ω_m using the HSC-Y1 data. We compare the posterior of these parameters calculated using both the angular power spectrum C_ℓ^{KK} (red contours), the Minkowski functionals (blue contours), and the combination of these statistics (green contours). For the two-point statistics only, C_ℓ^{KK} constraints for Ω_m are prior dominated, whereas $S_8 = 0.790^{+0.077}_{-0.057}$, which is consistent with previous results (e.g. [Hikage et al. 2019](#)). Including Minkowski functionals in the analysis results in tighter constraints, with a significant improvement on S_8 . The marginal posterior of the combined statistics yields $\Omega_m = 0.293^{+0.157}_{-0.043}$ and $S_8 = 0.808^{+0.033}_{-0.046}$, roughly a 40% tighter than using the power spectrum only for S_8 . It is worth noticing that using only the Minkowski functional for the inference, results in virtually the same constraints improvements for $S_8 = 0.819^{+0.032}_{-0.048}$. From these results, we also find noticeable constraints on Ω_m from the combination of our statistics, indicating the power of Minkowski functionals to break degeneracy between S_8 and Ω_m , which is not possible from two-point statistics only. These results show agreement with different non-Gaussian probes on the same dataset.

8 SUMMARY & CONCLUSIONS

We apply Minkowski functionals, a type of non-Gaussian statistic, to convergence maps built from the HSC-Y1 dataset, obtaining new constraints on S_8 and Ω_m . We combine these measurements with two-point statistics, utilizing measurements of the angular power spectrum of convergence C_ℓ^{KK} to improve the results from two-point functions only. Using a likelihood approach based on emulated simulation predictions, with different S_8 and Ω_m , we do a full posterior analysis to find constraints on these cosmological parameters. Before un-blinding the data, we calibrate scale cuts on the individual data vectors and Gaussian smoothing scales of the maps to mitigate biases coming from systematic effects that can affect the final results once we include small scale modes. However, no significant shift is found for the studied systematics, which indicates these are effectively controlled by our scale cut choices. This is in agreement with results from [Grandón et al. \(2024\)](#), which investigates the effect of baryon in several non-Gaussian statistics for HSC-Y1 dataset in the same regime used for this study. Additionally, we test the robustness of our analysis by checking the self-consistency of this probe, by measuring different choices of the data vector, including constraints using individual Minkowski functionals, adding additional smoothing scales, removing part of the data vector, and removing individual tomographic redshift bins. The baseline analysis includes V_0 , V_1 and V_2 , combined with measurements of C_ℓ at $300 < \ell < 1000$, with a smoothing scale of $\theta = 2'$, yielding $S_8 = 0.808^{+0.033}_{-0.046}$, consistent with other probes of non-Gaussian statistics using HSC-Y1 data and with the S_8 inferred by the CMB probes. This value for S_8 represents a 40% improvement in comparison to the constraint provided by power spectrum only. Also, the constraint $\Omega_m = 0.293^{+0.157}_{-0.043}$ is found with similar results to the ones presented in [Marques et al. \(2024\)](#) and [Cheng et al. \(2024\)](#), using peak statistics and scattering transform, showing the improved performance of these statistics to break degeneracy between Ω_m and σ_8 . Also, the final constraints are fully consistent with [Novaes et al. \(2024\)](#), which uses a differ-

ent compression method for the data vector and a machine-learning based method for the posterior estimation.

In contrast to the power spectrum that can fully characterize a random Gaussian fields, Minkowski functionals are a way to encapsulate the information from non-Gaussianity terms (Matsubara 2003). We find that most of the constraining power on Ω_m and S_8 from our combined statistic, comes from the area V_0 and perimeter V_1 , each with very similar constraining power, but a with better constraint of Ω_m given by V_1 . Moreover, for the genus V_2 these constraints are wider, which indicates this particular Minkowski functional capturing less non-Gaussian information from the HSC dataset. We believe that statistical errors and data noise are relevant and have a higher impact on V_2 , in particular on the second and third derivatives of the skewness parameter S_1 and S_2 , which contribute to the non-Gaussian information of V_2 (Petri et al. 2013), indicating a larger impact to of noise, to the one quantified in Matsubara & Jain (2001). In fact, Shirasaki et al. (2013) shows that even though is a robust measurement, either cosmic variance or statistical error may affect on the individual Minkowski functionals. Additionally, a similar tendency is found in Petri et al. (2013); Petri et al. (2015), with V_2 providing less constraining power in comparison to V_0 and V_1 , and showing a slow convergence of the perturbative series for small smoothing scales ($\theta < 15'$), such as the ones used in this study. Regardless, removing V_2 from the analysis does not improve the constraints. Additionally, the analysis shows that the most constraining power comes from the third redshift bin z_3 of the data, because of the larger sample this particular redshift bin provides. The same tendency found in the previous studies using the HSC-Y1 data.

In general, these results improve the previous constraints from Petri et al. (2015) using the CFHTLenS dataset, where a similar approach using emulation is used to model the cosmological dependence of Minkowski functionals. Our study finds no biases in the constraints results for the (Ω_m , σ_8). However, their analysis is also extended to more cosmological parameters, such as the dark energy equation of state w , which can drive the bias found in their study.

Finally, we believe that future analyses using Stage-IV galaxy surveys, such as Vera Rubin Observatory Legacy Survey of Space and Time (LSST; Ivezić et al. 2019), Euclid (Laureijs et al. 2011), and Nancy Grace Roman Space Telescope (Eifler et al. 2021), with a better control of the photometric redshifts and larger surveyed area, will provide a more accurate result.

ACKNOWLEDGEMENTS

JA thanks useful discussion with Surhud More, Linda Blot, Joachim Harnois-Déraps and Masahiro Takada. JA is supported by JSPS KAKENHI Grant Number JP23K19064. MS is in part supported by MEXT KAKENHI Grant Number (20H05861, 23K19070, 24H00215, 24H00221). CPN thanks Instituto Serrapilheira for financial support. Numerical computations were in part carried out on Cray XC50 at Center for Computational Astrophysics, National Astronomical Observatory of Japan. This work was supported by JSPS KAKENHI Grants 23K13095 and 23H00107 (to JL). This research used computing resources at Kavli IPMU. This research used resources at the National Energy Research Scientific Computing Center (NERSC), a U.S. Department of Energy Office of Science User Facility located at Lawrence Berkeley National Laboratory, operated under Contract No. DE-AC02-05CH11231. The Kavli IPMU is supported by the WPI (World Premier International Research Center) Initiative of the MEXT (Japanese Ministry of Education, Culture, Sports, Science and Technology). This manuscript has been

authored by Fermi Research Alliance, LLC under Contract No. DE-AC02-07CH11359 with the U.S. Department of Energy, Office of Science, Office of High Energy Physics.

DATA AVAILABILITY

The HSC-Y1 data is publicly available. The simulations and the generated mock catalogues used in this paper are available on reasonable request.

REFERENCES

- Adler R. J., 2014, *Random Fields*. John Wiley & Sons, Ltd (<https://onlinelibrary.wiley.com/doi/pdf/10.1002/9781118445112.stat02991>), doi:<https://doi.org/10.1002/9781118445112.stat02991>, <https://onlinelibrary.wiley.com/doi/abs/10.1002/9781118445112.stat02991>
- Albrecht A., et al., 2006, arXiv preprint astro-ph/0609591
- Amon A., et al., 2022, *Phys. Rev. D*, **105**, 023514
- Anbajagane D., et al., 2023, *Monthly Notices of the Royal Astronomical Society*, **526**, 5530
- Appleby S., Park C., Pranav P., Hong S. E., Hwang H. S., Kim J., Buchert T., 2022, *The Astrophysical Journal*, **928**, 108
- Bianchini F., et al., 2020, *ApJ*, **888**, 119
- Boyle A., Uhlemann C., Friedrich O., Barthelemy A., Codis S., Bernardeau F., Giocoli C., Baldi M., 2021, *MNRAS*, **505**, 2886
- Bridle S., King L., 2007, *New Journal of Physics*, **9**, 444
- Burger P. A., et al., 2023, *A&A*, **669**, A69
- Cheng S., Marques G. A., Grandón D., Thiele L., Shirasaki M., Ménard B., Liu J., 2024, arXiv e-prints, p. arXiv:2404.16085
- Dark Energy Survey Collaboration et al., 2016, *Monthly Notices of the Royal Astronomical Society*, **460**, 1270
- Davies C. T., Cautun M., Giblin B., Li B., Harnois-Déraps J., Cai Y.-C., 2022, *MNRAS*, **513**, 4729
- Duque J. C., Carones A., Marinucci D., Migliaccio M., Vittorio N., 2024, *Journal of Cosmology and Astroparticle Physics*, **2024**, 039
- Eifler T., et al., 2021, *MNRAS*, **507**, 1746
- Feldbrugge J., van Engelen M., van de Weygaert R., Pranav P., Vegter G., 2019, *Journal of Cosmology and Astroparticle Physics*, **2019**, 052
- Fluri J., Kacprzak T., Refregier A., Amara A., Lucchi A., Hofmann T., 2018, *Phys. Rev. D*, **98**, 123518
- Fluri J., Kacprzak T., Lucchi A., Schneider A., Refregier A., Hofmann T., 2022, *Phys. Rev. D*, **105**, 083518
- Fu L., et al., 2014, *MNRAS*, **441**, 2725
- Gatti M., et al., 2024, *Physical Review D*, **109**, 063534
- Giblin B., et al., 2021, *A&A*, **645**, A105
- Grandón D., Marques G. A., Thiele L., Cheng S., Shirasaki M., Liu J., 2024, arXiv e-prints, p. arXiv:2403.03807
- Grewal N., Zuntz J., Tröster T., Amon A., 2022, *The Open Journal of Astrophysics*, **5**, 13
- Gruen D., et al., 2018, *Phys. Rev. D*, **98**, 023507
- Gupta A., Zorrilla Matilla J. M., Hsu D., Haiman Z., 2018, *Phys. Rev. D*, **97**, 103515
- Halder A., Gong Z., Barreira A., Friedrich O., Seitz S., Gruen D., 2023, *J. Cosmology Astropart. Phys.*, **2023**, 028
- Hamann J., Kang Y., 2024, *J. Cosmology Astropart. Phys.*, **2024**, 076
- Harnois-Déraps J., Martinet N., Reischke R., 2021, *Monthly Notices of the Royal Astronomical Society*, **509**, 3868
- Heavens A. F., Jimenez R., Lahav O., 2000, *Monthly Notices of the Royal Astronomical Society*, **317**, 965
- Heavens A. F., Sellentin E., de Mijolla D., Vianello A., 2017, *Monthly Notices of the Royal Astronomical Society*, **472**, 4244
- Heymans C., et al., 2012, *MNRAS*, **427**, 146
- Hikage C., Matsubara T., 2012, *MNRAS*, **425**, 2187
- Hikage C., et al., 2003, *PASJ*, **55**, 911

- Hikage C., Komatsu E., Matsubara T., 2006, [ApJ](#), **653**, 11
- Hikage C., Coles P., Grossi M., Moscardini L., Dolag K., Branchini E., Matarrese S., 2008a, [MNRAS](#), **385**, 1613
- Hikage C., Matsubara T., Coles P., Liguori M., Hansen F. K., Matarrese S., 2008b, [MNRAS](#), **389**, 1439
- Hikage C., et al., 2019, [Publications of the Astronomical Society of Japan](#), **71**, 43
- Hildebrandt H., et al., 2017, [MNRAS](#), **465**, 1454
- Hildebrandt H., et al., 2020, [A&A](#), **633**, A69
- Hildebrandt H., et al., 2021, [A&A](#), **647**, A124
- Hinshaw G., et al., 2013, [The Astrophysical Journal Supplement Series](#), **208**, 19
- Ivezic Ž., et al., 2019, [ApJ](#), **873**, 111
- Jiang A., Liu W., Fang W., Li B., Barrera-Hinojosa C., Zhang Y., 2024, [Phys. Rev. D](#), **109**, 083537
- Kaiser N., Squires G., 1993, [ApJ](#), **404**, 441
- Kilbinger M., 2015, [Reports on Progress in Physics](#), **78**, 086901
- Kratochvil J. M., Lim E. A., Wang S., Haiman Z., May M., Huffenberger K., 2012, [Phys. Rev. D](#), **85**, 103513
- Laureijs R., et al., 2011, [arXiv e-prints](#), p. [arXiv:1110.3193](#)
- Li X., et al., 2022, [PASJ](#), **74**, 421
- Lim E. A., Simon D., 2012, [J. Cosmology Astropart. Phys.](#), **2012**, 048
- Liu J., Madhavacheril M. S., 2019, [Phys. Rev. D](#), **99**, 083508
- Liu X., Yuan S., Pan C., Zhang T., Wang Q., Fan Z., 2023a, [MNRAS](#), **519**, 594
- Liu W., Jiang A., Fang W., 2023b, [J. Cosmology Astropart. Phys.](#), **2023**, 037
- Madhavacheril M. S., Smith K. M., Sherwin B. D., Naess S., 2020, [arXiv e-prints](#), p. [arXiv:2011.02475](#)
- Mandelbaum R., 2018, [ARA&A](#), **56**, 393
- Mandelbaum R., et al., 2017, [Publications of the Astronomical Society of Japan](#), **70**, S25
- Mandelbaum R., et al., 2018, [MNRAS](#), **481**, 3170
- Marques G. A., Liu J., Zorrilla Matilla J. M., Haiman Z., Bernui A., Novaes C. P., 2019, [J. Cosmology Astropart. Phys.](#), **2019**, 019
- Marques G. A., et al., 2024, [MNRAS](#), **528**, 4513
- Matsubara T., 2003, [The Astrophysical Journal](#), **584**, 1
- Matsubara T., Jain B., 2001, [ApJ](#), **552**, L89
- Mecke K. R., Buchert T., Wagner H., 1994, [A&A](#), **288**, 697
- Melchior P., Viola M., 2012, [Monthly Notices of the Royal Astronomical Society](#), **424**, 2757
- Nelson D., et al., 2019, [Computational Astrophysics and Cosmology](#), **6**, 2
- Novaes C. P., Bernui A., Marques G. A., Ferreira I. S., 2016, [Monthly Notices of the Royal Astronomical Society](#), **461**, 1363
- Novaes C. P., et al., 2024, Cosmology from HSC Y1 Weak Lensing with Combined Higher-Order Statistics and Simulation-based Inference ([arXiv:2409.01301](#)), [https://arxiv.org/abs/2409.01301](#)
- Osato K., Liu J., Haiman Z., 2021, [MNRAS](#), **502**, 5593
- Paillas E., et al., 2024, [MNRAS](#), **531**, 898
- Petri A., Haiman Z., Hui L., May M., Kratochvil J. M., 2013, [Phys. Rev. D](#), **88**, 123002
- Petri A., Liu J., Haiman Z., May M., Hui L., Kratochvil J. M., 2015, [Phys. Rev. D](#), **91**, 103511
- Pires S., Starck J.-L., Amara A., Teyssier R., Réfrégier A., Fadili J., 2009, [Monthly Notices of the Royal Astronomical Society](#), **395**, 1265
- Planck Collaboration et al., 2020, [A&A](#), **641**, A6
- Sato J., Takada M., Jing Y. P., Futamase T., 2001, [ApJ](#), **551**, L5
- Schimd C., Kraljic K., Davé R., Pichon C., 2024, [A&A](#), **689**, A311
- Schmalzing J., Buchert T., 1997, [ApJ](#), **482**, L1
- Schmalzing J., Kerscher M., Buchert T., 1996, in Bonometto S., Primack J. R., Provenzale A., eds, *Dark Matter in the Universe*. p. 281 ([arXiv:astro-ph/9508154](#)), [doi:10.48550/arXiv.astro-ph/9508154](#)
- Shirasaki M., Yoshida N., 2014, [ApJ](#), **786**, 43
- Shirasaki M., Yoshida N., Hamana T., Nishimichi T., 2012, [ApJ](#), **760**, 45
- Shirasaki M., Yoshida N., Hamana T., 2013, [ApJ](#), **774**, 111
- Shirasaki M., Nishimichi T., Li B., Higuchi Y., 2017, [MNRAS](#), **466**, 2402
- Shirasaki M., Hamana T., Takada M., Takahashi R., Miyatake H., 2019, [Monthly Notices of the Royal Astronomical Society](#), **486**, 52
- Shirasaki M., Moriwaki K., Oogi T., Yoshida N., Ikeda S., Nishimichi T., 2021, [Monthly Notices of the Royal Astronomical Society](#), **504**, 1825
- Spina B., Porciani C., Schimd C., 2021, [Monthly Notices of the Royal Astronomical Society](#), **505**, 3492
- Starck J. L., Themelis K. E., Jeffrey N., Peel A., Lanusse F., 2021, [A&A](#), **649**, A99
- Takada M., Jain B., 2003, [Monthly Notices of the Royal Astronomical Society](#), **344**, 857
- Takahashi R., Hamana T., Shirasaki M., Namikawa T., Nishimichi T., Osato K., Shiroyama K., 2017, [ApJ](#), **850**, 24
- Tanaka M., et al., 2018, [PASJ](#), **70**, S9
- Thiele L., Marques G. A., Liu J., Shirasaki M., 2023, [Phys. Rev. D](#), **108**, 123526
- Tomita H., 1986, [Progress of Theoretical Physics](#), **76**, 952
- Troxel M. A., et al., 2018, [Phys. Rev. D](#), **98**, 043528
- Valogiannis G., Yuan S., Dvorkin C., 2024, [Phys. Rev. D](#), **109**, 103503
- Zhong K., Gatti M., Jain B., 2024, [arXiv e-prints](#), p. [arXiv:2403.01368](#)
- Zürcher D., et al., 2022, [MNRAS](#), **511**, 2075

This paper has been typeset from a \LaTeX file prepared by the author.